

# Removal and Recovery of Ammonia from Wastewater using $Ti_3C_2T_x$ MXene in Flow Electrode Capacitive Deionization

Naqsh E Mansoor<sup>1</sup>, Luis A. Diaz Aldana<sup>2</sup>, Christopher E. Shuck<sup>3</sup>, Yury Gogotsi<sup>3</sup>, Tedd E. Lister<sup>2,\*</sup>, and David Estrada<sup>1,4,\*</sup>

<sup>1</sup> Micron School of Materials Science and Engineering, Boise State University, Boise, ID 83725, USA

<sup>2</sup> Idaho National Laboratory, Idaho Falls, ID 83401, USA

<sup>3</sup>A.J. Drexel Nanomaterials Institute and Department of Materials Science and Engineering, Drexel University, Philadelphia, PA 19104

<sup>4</sup> Center for Advanced Energy Studies, Boise State University, Boise, ID 83725, USA

\*Corresponding authors: [tedd.lister@inl.gov](mailto:tedd.lister@inl.gov), [daveestrada@boisestate.edu](mailto:daveestrada@boisestate.edu)

## 3.1. Abstract

Flow electrode CDI systems (FE-CDI) have recently garnered attention because of their ability to prevent cross contamination, and operate in uninterrupted cycles ad infinitum. Typically, FE-CDI electrodes suffer from low conductivity, which reduces deionization performance. Higher mass loading to combat low conductivity leads to poor rheological properties, which prevent the process from being continuous and scalable. Herein,  $Ti_3C_2T_x$  MXenes were introduced as 1 mg/mL slurry electrodes in an FE-CDI system for the removal and recovery of ammonia from stimulated wastewater. The electrode performance was evaluated by operating the FE-CDI system with a feed solution of 500 mg/L  $NH_4Cl$  running in batch mode at a constant voltage of 1.2 and -1.2 V in charging and discharging modes respectively. Despite low loading compared to activated carbon solution,  $Ti_3C_2T_x$  flowing electrodes showed markedly improved performance by achieving 60% ion removal efficiency in a saturation time of 115 minutes, and an unprecedented adsorption capacity of 460 mg/g. The system proved to be a green technology by exhibiting satisfactory charge efficiency of 58-70% while operating at a relatively low energy consumption of 0.45 kWh/kg when compared to the current industry standard nitrification-denitrification ammonia stripping process. A 92% regeneration efficiency showed that the electrodes were stable and suitable for long term and scalable usage. The results demonstrate that MXenes hold great

potential in improving the FE-CDI process for energy-efficient removal and recovery of ammonium ions from wastewater.

### 3.2. Introduction

Energy and water exist in a complex symbiotic relationship; energy production has a water footprint, while water remediation and supply efforts exert a strain on the power resources. Nuclear and coal power plants require between 20 to 60 gallons of freshwater for every kilowatt-hour (kWh) of energy generated [1]. Correspondingly, water remediation and recovery efforts consume 2% of the total energy generated in the United States [2][3]. Environmental efficiency and economics encourage conservation of both resources. Water itself is an abundant resource but only 2.5% is readily accessible as freshwater, and there are already countries that rely on remediation efforts to obtain their water supply [4]. As the global population continues to rise, energy and water consumption will increase while existing natural sources will continue to be depleted. In its annual 2019 report, the International Energy Agency (IEA) predicts an 85% increase in energy related water usage in the upcoming years [3]. In light of this projection [3], it is imperative that versatile, cost-effective, and energy-efficient water technologies are developed. Wastewater reclamation is one step in a multi-stage solution to solve the looming freshwater availability crisis. Wastewater reclamation is environmentally as well as fiscally relevant because it can yield purified effluent, as well as recover embedded resources.

Ammonia is one of the most common contaminants found in domestic and industrial wastewaters. Yet, due to its importance in the agricultural industry, ammonia is one of the most industrially produced chemicals, with over 14 million metric tons produced in the United States alone in 2019 [5][6]. The production of ammonia requires copious amounts of both energy and water. While ammonia is undeniably a valuable building block in the modern food production, excessive exposure is a valid concern, due to its toxicity [5][7]. The release of ammonia rich wastewater to aquatic ecosystems can cause eutrophication, leading to disruptions in delicate ecological balances [8]. Owing to these detrimental effects, the Clean Water Act (CWA) prohibits industrial facilities from releasing nitrogen (as ammonia) rich wastewater to waterbodies [9]. Considerable effort has been devoted to developing efficient ammonia removal methodologies [10]. Despite that, biological nitrification remains the most widespread method for treating ammonia wastewater [11]. Aside from being cumbersome and slow, it also wastes embedded ammonia, which is otherwise a valuable product. In pursuit of sustainability, product conservation directly translates to energy conservation. Hence, there remains room for a technology that is energy, water, and resource efficient.

Prevalent water remediation technologies such as reverse osmosis, multiple effect distillation, and multistage flash distillation require anywhere from 2-58 kWh/m<sup>3</sup> of direct energy input [12]. Reverse Osmosis (RO) is the most common technique, and typically uses 2-10 kWh/m<sup>3</sup> of power [13]. Among purification technologies, capacitive deionization (CDI) has been a promising contender. It is an electrophoretic technique that uses a small voltage (~ 1.2 V) applied across two high surface area electrodes to induce charge separation. Similar to a supercapacitor, the charges are stored in the electric double layer of the electrodes. Even though there has been increasing research interest in CDI [14], the unavailability of adequate electrode materials acts as a bottleneck for the technology. Since voltage reversal (or removal), causes desorption of the immobilized ions, the technique can be used for purification as well as retrieval. Several studies report high water recovery (80-90%) and low energy utilization (0.6 kWh/m<sup>3</sup>) for desalination using CDI [15]–[17].

As a result of an increased research activity around CDI [14], several different cell architectures have been developed including inverted-, hybrid-, ultrafiltration-, flow-by-, desalination battery, membrane-, flow-through-, cation intercalation desalination, and flow-electrode CDI (FE-CDI) [18]. Apart from FE-CDI, all of these cell architectures utilize stationary electrodes and hence require an additional regeneration step for ion desorption, leading to non-continuous operation [18], [19]. Additionally, the regeneration step can cause cross-contamination between the effluent streams, resulting in lower water recovery [20]. This step negatively affects the fundamental motivators for CDI technology: cost, time, and energy efficiency. Due to the ability to regenerate electrodes simultaneously, FE-CDI is a pioneering electrochemical technology that promises continuous, infinite remediation even for high concentration feed waters [21]. The adsorption capacity of the system is controlled by regulating the flow rate, channel design, and the nature and loading of the electrode material.

Carbon and its derivatives such as graphene sponge, graphene oxide, carbon nanotubes (CNTs), and various composites have been investigated as CDI electrodes [22]. Carbon serves as an excellent prototype material due to its high surface area, electrical conductivity, and electrochemical stability [22]. While carbon materials have been shown to perform well in stationary electrode cell architectures [23], they suffer from low electrical conductivity in a slurry electrode systems [24]. In prior studies, and in our experimental experience, remediating the conductivity problem by increasing carbon content (> 15 wt.%) leads to clogged flow channels, halting operation.

MXenes are a class of two-dimensional (2D) transition metal carbides, nitrides and carbonitrides with the general formula  $M_{n+1}X_nT_x$  where M is an early transition metal (Ti, V, Nb, etc.), X is carbon and/or nitrogen,  $T_x$  represents the surface terminations (=O, -F, -Cl, and -OH), and  $n = 1-4$  [25]. The family of materials is highly conductive, hydrophilic, and can be scalably produced with no loss of properties [26], [27]. MXenes have already been proposed as materials useful for environmental remediation, including heavy metal adsorption, pollutant adsorption, desalination, amongst others [28], [29].  $Ti_3C_2T_x$  was the first MXene discovered and is the most widely studied [30]. Furthermore,  $Ti_3C_2T_x$  was shown to pose no ecological risk to aquatic ecosystems [31]. Recently this material has been applied to conventional CDI owing to high surface area and electrical properties [32]–[36].

Many studies have shown that  $Ti_3C_2T_x$  is a promising pseudocapactive anode for supercapacitors [37]–[40]. Ideal materials for aqueous electrochemical energy storage should have high specific capacitance, charge efficiency, and electrochemical stability at water electrolysis potential (~ 1.23V) [41], [42]. These features are also required in high performance CDI electrodes, suggesting that  $Ti_3C_2T_x$  will be appropriate for CDI systems. Wang et al. demonstrated the use of aerogel-like  $Ti_3C_2T_x$  MXene electrodes in a conventional desalination CDI cell to report an unprecedented salt adsorption capacity of 45 mg/g [43]. In a recent publication, Ma et al. used binder free pristine  $Ti_3C_2T_x$  films to achieve a salt adsorption capacity of 68 mg/g [32]. However, conventional CDI cells invariably experience co-ion expulsion, which reduces their charge efficiency [44]. The necessity of a regeneration step in conventional CDI invariably increases energy consumption [19], [20]. For CDI to be considered a green technology, it is necessary to account for the operating energy. The use of ion exchange membranes in the cell reduces co-ion expulsion. High charge efficiency leads to low operating energy. With energy, water, and resource conservation, FE-CDI holds the promise to surpass the limitations of the preceding water remediation technologies including the widespread RO systems.

In the present study, we aim to evaluate the de-ammonification performance of  $Ti_3C_2T_x$  flow electrodes in an FE-CDI system. This has been schematically shown in Fig. 1. This work demonstrates the suitability of  $Ti_3C_2T_x$  MXenes as high performance, low loading flow electrodes. It also opens avenues for further exploration in using other MXenes in CDI technology.

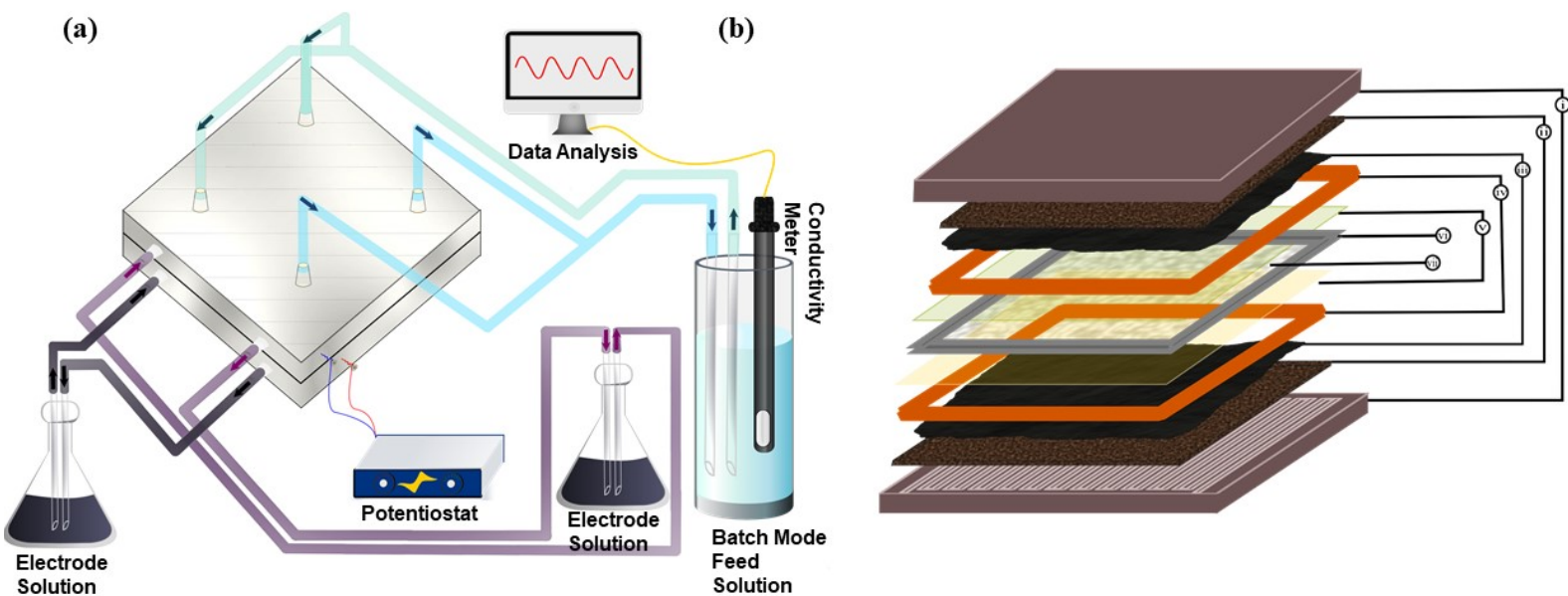


**Fig. 1. Schematic illustration for (a) FE-CDI module for deionization testing, and (b) CDI unit cell assembled with: i) Titanium Current Collectors ii) Vitreous Carbon iii) Carbon Cloth iv) Rubber Gaskets v) Anion and Cation Exchange Membranes vi) Spacer vii) Polyester Filter Felt.**

### 3.3 Experimental

#### 3.3.1. Preparation of Activated Carbon Flow Electrodes

The 10 wt.% control flow electrodes were prepared by mixing 1.2 g of 80 mesh activated carbon (AC) powder (Cabot Norit® A Ultra E 153) in 12 mL of nanopure water and stirring for 2 hours. The mixture was probe sonicated for 1 hour at 55 W to reduce the particle size by breaking up agglomerates, increasing the flowability. During cell operation, the electrodes were continuously stirred using a magnetic stir bar to prevent sedimentation of the carbon particles.

### 3.3.2. Preparation of $\text{Ti}_3\text{C}_2\text{T}_x$ Flow Electrodes

$\text{Ti}_3\text{C}_2\text{T}_x$  MXenes were etched from commercially obtained  $\text{Ti}_3\text{AlC}_2$  MAX Phase (2D Semi-Conductors) using the minimally intensive layer delamination (MILD) synthesis method [38]. This method was selected because of its reduced toxicity, and the ability to produce low defect, larger MXene flakes [45], [46]. 20 mL of 9 M hydrochloric acid (HCl, Alfa Aesar) was stirred with 1.6 g of Lithium Fluoride (LiF, 99.85% Alfa Aesar) using a Teflon magnetic bar at 300 rpm for 10 minutes prior to addition of the MAX. 1 g of  $\text{Ti}_3\text{AlC}_2$  was added to the *in-situ* synthesized HF solution in four increments to prevent overheating of the solution. The reaction was allowed to run for 24 hours at room temperature and ambient pressure (RTP). The resultant mixture was then washed using nanopure water via centrifugation at 3500 rpm until the acidic supernatant became neutral (pH 5-6). The presence of lithium ions ( $\text{Li}^+$ ) with the etching solution causes simultaneous etching/delamination resulting in an electrostatically stable colloidal solution. The stable supernatant was vacuum filtered with a glass microfiber filter (0.45  $\mu\text{m}$ , Whatman) to separate the MXene clay. To prepare the flow electrode solution, the MXene residue was re-dispersed in nanopure water via manual shaking to obtain a solution with concentration of 1 mg/mL (0.1 wt.%).

### 3.3.3. Characterization of $\text{Ti}_3\text{C}_2\text{T}_x$

To evaluate the morphology and structure of the samples, several characterization techniques were employed. X-ray diffraction (XRD) was conducted on a Rigaku Smartlab with equipped with a Cu  $\text{K}\alpha$  source, a step size of  $0.03^\circ$ , and a holding time of 0.5 s from  $3-90^\circ$ . The characteristic expanded structure of the MXenes was observed via scanning electron microscopy (SEM) and transmission electron microscopy (TEM) imaging on the FEI Teneo Field Emission SEM and JEOL JEM-2100 HR analytical TEM respectively. Microscopic imaging was also used to map out lateral size of the flakes, which was further confirmed by dynamic light scattering (DLS) performed on a Brookhaven NanoBrook Omni. The obtained measurement is the hydrodynamic diameter, where the particle is assumed to be spherical in nature. It is a function of diffusion co-efficient according to the Stokes-Einstein relation. The measurement is an effective average, and hence can deviate from actual lateral flake size. The tool was also used to measure electrophoretic mobility of the colloidal suspension. All measurements were taken at RTP (25  $^\circ\text{C}$ , 1 atm) and at 7 pH. The viscosity of the colloidal suspension was measured on a RheoSense  $\mu\text{Visc}$  Viscometer with 300  $\mu\text{L}$  of solution to obtain five repeated measurements. Raman spectra was obtained using a 532 nm He-Cd laser on a Horiba LabRAM HR Evolution Raman by drop casting the electrode solution on a glass slide.

### 3.3.4. Capacitive Deionization Experiments

To evaluate the performance of the electrodes, a self-assembled CDI unit with titanium current collectors of dimensions 6.35 cm x 6.35, carved with serpentine flow channels, was operated in batch mode in constant voltage (1.2 V) cycle in both charging and discharging stages. The power was sourced from a Biologic SP-50 potentiostat. The effective contact area was 10 cm<sup>2</sup>. As shown in Fig. 1.a, the cell was assembled with vitreous carbon (Duocel Reticulated Vitreous Carbon 100 ppi), carbon cloth (AvCarb 1071 HCB), rubber gaskets (Neoprene, 1.5 mm), along with pre-treated anion and cation exchange membranes (Fumasep FAA-3-PK-130 and Nafion™ 115 respectively). These were separated by a non-conductive porous spacer (Nylon 3/64") with a polyester filter felt (50 μm) that allowed the feed water to pass through. 20 mL of 0.5 mg/L ammonium chloride (NH<sub>4</sub>Cl) solution was prepared by dissolving analytical grade NH<sub>4</sub>Cl (99.99% Sigma Aldrich) in deionized water (18 MΩ-cm). The solution was circulated through the cell at a flow rate of 2 mL/min while a conductivity meter (HACH H1440d Benchtop Meter) monitored the conductivity of the NH<sub>4</sub>Cl solution. 6 mL each of the two electrode solutions were circulated in the cell channels at a flow rate of 3 mL/min.

### 3.3.5. Performance Metrics

To evaluate the performance of Ti<sub>3</sub>C<sub>2</sub>T<sub>x</sub> MXene (and AC) electrodes in the FE-CDI cell, the following equations were used to calculate the given metrics [47]:

- I. Conductivity ratio,  $C_f/C_o = \frac{c_o - c_f}{c_o}$
- II. Deionization efficiency =  $\frac{c_o - c_f}{c_o} \times 100\%$
- III. Deionization capacity,  $\Gamma = \frac{(c_o - c_f)(Vol)}{m} \text{ mg/g}$
- IV. Adsorption rate =  $\frac{(c_o - c_f)(Vol)}{At_{adsorb}} \text{ mg/min/cm}^2$
- V. Charge Efficiency,  $\Lambda = \frac{(F)(\Delta M)}{Q_{in}} \%$
- VI. Coulombic efficiency loss,  $\eta_{coul} = \frac{Q_{out}}{Q_{in}} \times 100\%$
- VII. Electrode regeneration efficiency,  $\eta_r = \frac{\Gamma_n}{\Gamma_i} \times 100\%$
- VIII. Energy Consumption =  $\frac{(V)(Q_{in})}{3600(c_o - c_f)_{adsorb}(Vol)} \text{ kWh/kg}$
- IX. Energy Recovery =  $\frac{(V)(Q_{out})}{3600(c_o - c_f)_{desorb}(Vol)} \Big/ \text{Energy Consumption} \times 100\%$

Where,

$C_o$  = Initial concentration of effluent solution (mg/L)

$C_f$  = Final concentration of effluent solution (mg/L)

Vol = Volume of feed solution (L)

m = Mass of particle loading in electrode slurry (g)

A = Contact area between electrode flow channel and ion-exchange membranes ( $\text{cm}^2$ )

t = Time of adsorption cycle (min)

$\Delta M$  = Moles of  $\text{NH}_4\text{Cl}$  removed (mol)

F = Faraday's constant (96485 C/mol)

$Q_{in}$  = Charge uptake during adsorption (C)

$Q_{out}$  = Charge release during desorption (C)

$\Gamma_n$  = Deionization capacity of the final cycle (mg/g)

$\Gamma_i$  = Deionization capacity of the initial cycle (mg/g)

V = Voltage applied across the cell (V)

## 3.4. Results and Discussion

### 3.4.1 Material Characterization

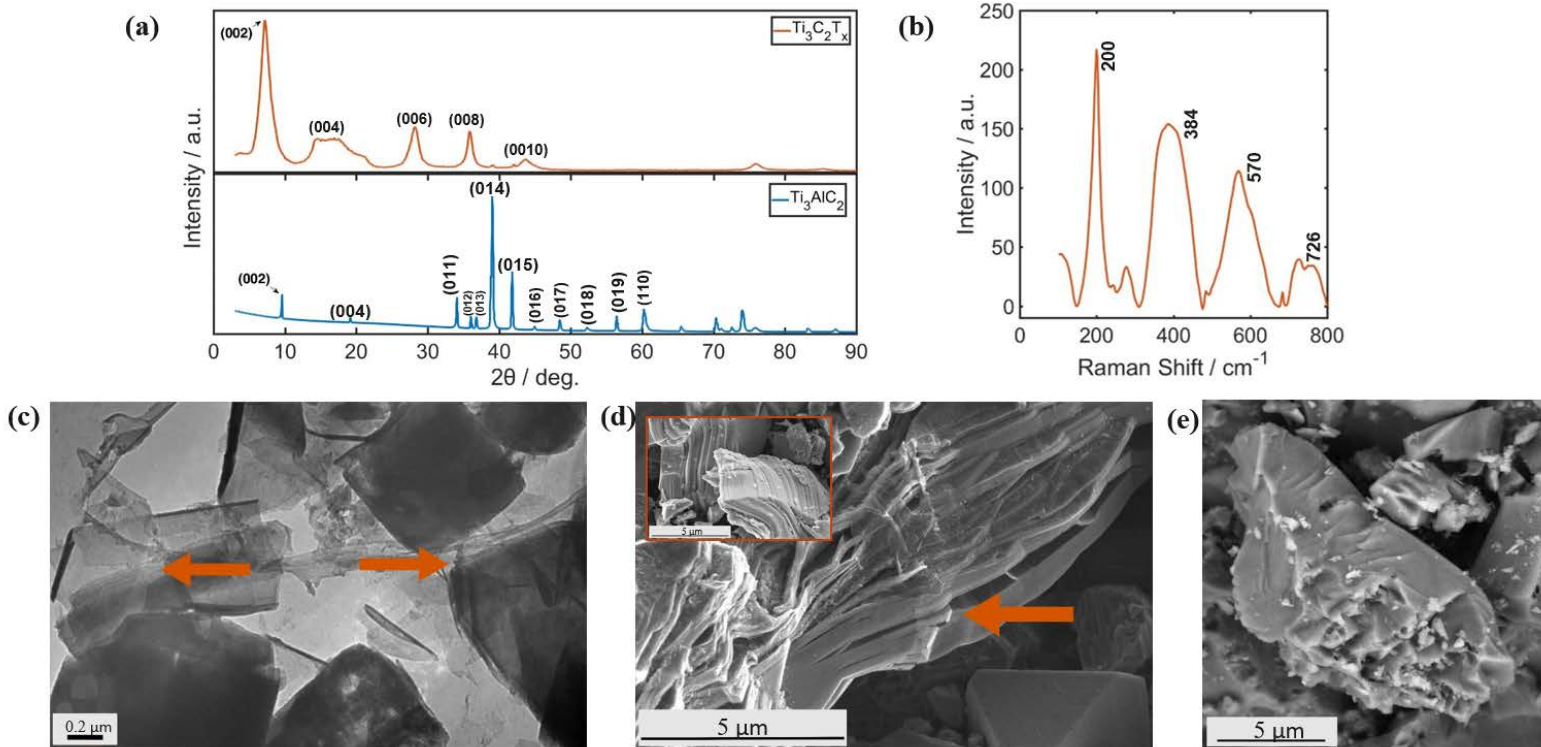


**Fig. 2. (a) XRD spectra of  $\text{Ti}_3\text{AlC}_2/\text{Ti}_3\text{C}_2\text{T}_x$  before and after etching; (b) Raman spectra of  $\text{Ti}_3\text{C}_2\text{T}_x$  flow electrodes at 532 nm; (c) TEM image of etched and delaminated  $\text{Ti}_3\text{C}_2\text{T}_x$  showing separated layers.; (d) SEM image of etched and delaminated  $\text{Ti}_3\text{C}_2\text{T}_x$  (inset) SEM image of  $\text{Ti}_3\text{AlC}_2$ ; (e) SEM image of AC powder particle**

XRD results shown in Fig. 2.a confirms successful etching of Aluminum (Al) from the  $\text{Ti}_3\text{AlC}_2$  MAX phase by the shift in the (002) peak from  $9.60^\circ$  to  $7.17^\circ$ . In the MILD method, etching and delamination simultaneously, with delamination occurring through intercalation of water ( $\text{H}_2\text{O}$ ), and lithium ions ( $\text{Li}^+$ ). The ion removal mechanism in FE-CDI is dependent on the type of electrode material used [14]. Carbon electrodes operate through ion adsorption on the charged surface of the particles, while MXenes function by allowing ion insertion between the individual sheets [48]. Hence, the interlayer spacing has a pronounced effect on the charge storage and the ionic transport properties of MXenes [49]. The etched  $\text{Ti}_3\text{C}_2\text{T}_x$  has a total interlayer spacing of  $4.40 \text{ \AA}$ , due to the intercalated water and lithium ions coupled with successful etching. The interlayer spacing determines if charge storage can occur via interaction. The ammonium ion has a diameter

of 3.50 Å, hence making it viable for it to intercalate. This results in the characteristic expanded structure of MXenes, as shown in Fig. 2.d.

The Raman spectra in Fig. 2.b shows four distinct characteristic peaks at 200, 384, 570, and 726  $\text{cm}^{-1}$ . The  $A_{1g}$  peak at 200  $\text{cm}^{-1}$  and the  $E_g$  peak at 384  $\text{cm}^{-1}$  correspond to vibrations due to surface groups on titanium. [50]. While the  $E_g$  and  $A_{1g}$  peaks observed at 570  $\text{cm}^{-1}$  and 726  $\text{cm}^{-1}$  respectively, can be attributed to carbon variations. [50]. The absence of sharp  $E_{g1}$  peak (at 144  $\text{cm}^{-1}$ ) and positive shifting of the spectra can be attributed to the nanosized structure of the flakes [30], [50]. Line broadening and merging in the spectra is indicative of exfoliation and delamination and is hence consistent with the XRD data.

TEM image in Fig. 2.c shows stacked multilayer MXene sheets that are thin and electron transparent. The morphology and surface structure of the electrode particle materials have a significant effect on the ion adsorption capacity. The highly accessible surface, characterized by the expanded and open interlayer structure, allow for rapid ion adsorption within the MXene sheets [51]. The porous structure of AC is clearly observed in Fig. 3.2.e. The figure also exhibits the irregular block morphology of AC, with particle size ranging in a few microns. This is consistent with DLS particle size analysis (Fig. 3.a). The characteristic fanned out basal planes of etched MXenes can be seen in Fig. 2.d. It can be witnessed visually that the spread out, open structure of MXenes has significantly more intercalating space than the porous structure of AC. Moreover, the unfurled morphology is evidence for successful etching of  $\text{Ti}_3\text{AlC}_2$  (Fig. 2.d-inset) and is hence in agreement with the aforementioned XRD and Raman results.

### 3.4.2. Flow Electrode Slurry Characterization

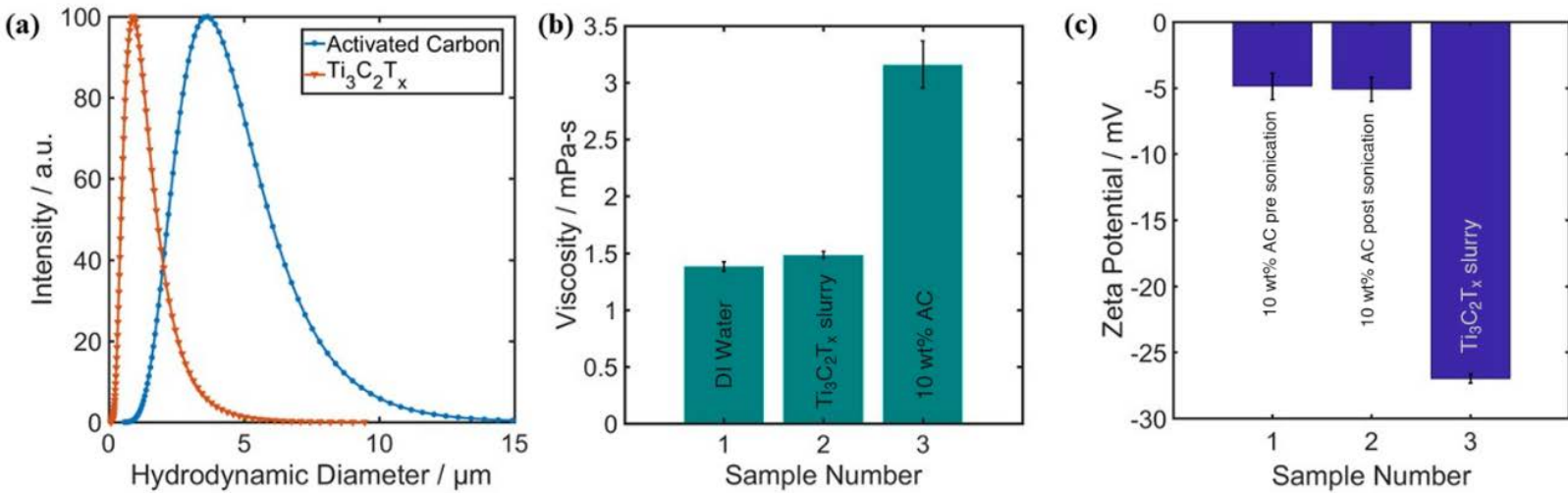


**Fig. 3. (a) Particle size analysis of 10 wt% AC slurry electrodes and  $\text{Ti}_3\text{C}_2\text{T}_x$  flow electrodes; (b) Viscosity measurements of 1. DI Water, 2.  $\text{Ti}_3\text{C}_2\text{T}_x$  flow electrodes, and 3. 10 wt% AC slurry electrodes; (c) Surface potential measurements of 1. 10 wt% AC slurry before sonication, 2. 10 wt% AC electrodes after sonication.**

The flow electrode is the most important component of the FE-CDI cell. The rheological properties and followability of the electrode contribute towards the deionization capacity, stability, and cyclicity of the system. Due to homogeneity, stable colloidal slurries perform better as flow electrodes. For colloidal suspensions, rheological properties are a function of the size and concentration of the added dispersant [52]. Fig. 3.a shows particle size profiles of the 10 wt.% AC slurry and the  $\text{Ti}_3\text{C}_2\text{T}_x$  electrodes. It is evident that the average particle size is lower for MXene electrodes (1.2  $\mu\text{m}$ ) than AC (4.5  $\mu\text{m}$ ). In addition, the AC profile exhibits a wider distribution and longer tail end, indicating particle flocculation. For this reason, the AC slurry was continuously stirred during the experiment to prevent sedimentation. Furthermore, the viscosity of a suspension has a strong correlation with particle size. Higher viscosity contributes to poor followability and dispersion of the slurry. Fig. 3.b shows that the  $\text{Ti}_3\text{C}_2\text{T}_x$  solution has a viscosity very close to deionized (DI) water (1.483 mPa-s and 1.382 mPa-s respectively). Experimentally, this resulted in excellent followability and zero hindrance during the cell operation. This can be attributed to the presence of hydrophilic functional groups on the surface of MXene layers which result in electrostatic repulsion that leads to a stable colloidal solution not prone to flocculation [27]. Comparatively, the third sample, AC slurry had a higher viscosity. Combined with larger particle

size (Fig. 3.a); it led to poor followability and frequent clogging of the narrow cell channels in our conductor design. Zeta ( $\zeta$ ) potential is an important guide to determine stability of suspensions. AC forms lyophobic colloids, which is reflected in its high (less negative)  $\zeta$ -potential value of -5 mV, as shown in Fig. 3.c. Sample 1 was prepared from as received 80 mesh AC powder, while sample 2 was probe sonicated for 1 hour to yield the particle size distribution given in Fig. 3.a. The two samples did not exhibit any considerable difference in  $\zeta$ -potential, as it is independent of particle size [52]. However, as aforementioned, reducing particle size had a positive impact on fluid flow. As apparent in Fig. 3.c, the  $\text{Ti}_3\text{C}_2\text{T}_x$  solution had a considerably lower (more negative)  $\zeta$ -potential value of -27 mV, which resulted in electrode stability throughout the CDI operation.

### 3.4.3. Deionization Performance Test

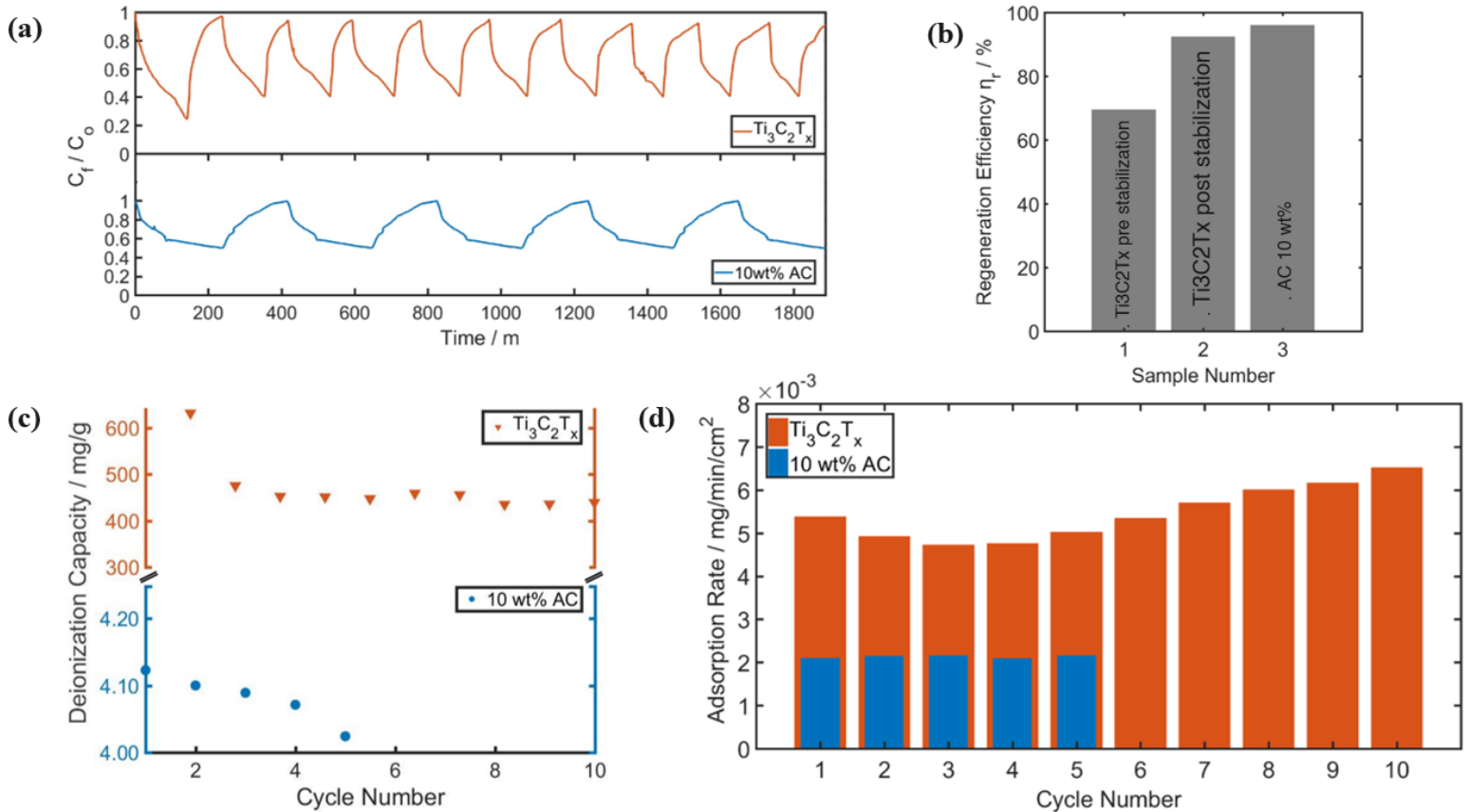


**Fig. 4. (a) Effluent conductivity showing electrosorption-desorption cycles; (b) Electrode regeneration efficiency of 1.  $Ti_3C_2T_x$  before stabilization 2.  $Ti_3C_2T_x$  after stabilization, and 3. AC; (c) Electrode adsorption capacity at each regenerative cycle; (d) Adsorption rate at each regenerative cycle.**

Fig. 4.a shows the change in conductivity ratio of the effluent solution as a function of time when the system was operated in batch mode. The observed cyclic conductivity change is representative of the ion capture and release steps during the regenerating operation. In this study, the 10 wt.% AC slurry was used as control electrodes to evaluate the performance of  $Ti_3C_2T_x$ . The conductivities of both deionization systems show a significant decrease with the application of 1.2 V external voltage. The open structure and intercalation capture mechanism in  $Ti_3C_2T_x$  MXenes resulted in a shorter saturation time of 115 minutes compared to AC (233 minutes), and other previously reported studies [53]–[55]. Due to the shorter charge-discharge times,  $Ti_3C_2T_x$  delivered 10 stable long-term cycles during the ~ 30 hour run time. This manifested in twice the number of cycles as AC (5 cycles). As saturated electrosorption is achieved, the

charging (ion capture) profile for  $Ti_3C_2T_x$  plateaus at an average conductivity ratio of 0.4070, which is lower than the obtained value for AC (0.5008). It is interesting to note that the conductivity ratio of the first run in cycle with  $Ti_3C_2T_x$  MXenes is markedly lower (0.2413) than the following cycles. In the first cycle, the system has not yet achieved dynamic equilibrium and the increased deionization is possibly a result of permanent chemical interactions on the defect sites on the MXene flakes [56]. These ions are not desorbed upon voltage reversal (or removal). Hence, the first cycle is not representative of the electrode performance. This is reflected in Fig. 4.b which shows electrode regeneration efficiency ( $\eta_r$ ). After achieving dynamic equilibrium (sample 2),  $\eta_r$  is upwards of 92%. If we take the first cycle into account,  $\eta_r$  drops to 69.5% which is evident of the suggestion that after the initial cycle, some adsorption sites are permanently occupied by chemical interactions. It is imperative to note that  $\eta_r$  for AC is slightly higher at 96%. This can be attributed to the oxidative and aqueous degradation of  $Ti_3C_2T_x$  MXenes over time [57]. However, researchers have been working to increase oxidative stability of MXenes [58]. In addition, the use of MXenes in non-aqueous solvents as flow electrodes can be explored in the future [59].

Deionization capacity is an integral criterion to evaluate the electrode performance in a FE-CDI cell. The average deionization capacities exhibit great disparity between the two electrode systems. The average removal capacity for  $Ti_3C_2T_x$  is 460 mg/g, or more than 2 orders of magnitude higher than AC, with average removal capacity of 4.2 mg/g. The values for each charge-discharge cycle are shown in Fig. 4.c. It can clearly be seen that deionization capacity decreases after the first cycle but then eventually stabilizes and remains nearly constant in the subsequent cycles. However, for  $Ti_3C_2T_x$  the lowest adsorption capacity (10<sup>th</sup> cycle) can still achieve a value of 439 mg/g, suggesting excellent regeneration stability (Fig. 4.b). In aqueous environments, the solvated ammonium ( $NH_4^+$ ) ions have an average radius of 0.331 nm [58], which is smaller than interlayer spacing (0.44 nm) of MXene sheets. The smaller hydrated radius can easily intercalate between the layers without kinetic limitation. Furthermore, with each cycle, the interlayer spacing is likely to increase to a higher value as the lithium ions are removed, which accounts for the increasing adsorption rate (Fig. 4.d). The removal of lithium ions lowers site competition making it easier for ammonia to intercalate. The significantly higher value of ammonia adsorption capacity follows the trend of previous studies [54], [60], where 2D materials, particularly graphene, show enhanced adsorption for ammonia compared to sodium chloride (NaCl) desalination. Graphene and graphene oxide (GO) possess similar structural features as MXenes but they lack surface functional groups and the natural hydrophilicity present in all MXenes. It has been established that ammonia interacts via a combination of physisorption and chemisorption [61]. The presence of the  $-OH$  and  $-O$  functional groups on the  $Ti_3C_2T_x$  surface

facilitate surface reactions with the  $\text{NH}_4^+$  ions. The surface chemistry and functional groups affect reactive adsorption as well as physical adsorption mechanisms [61]. In this study, we used a relatively high concentration (500 mg/L) feed solution as a stand-in for wastewater. Higher initial ionic concentrations enhance adsorption capacity [62]. In addition, the use of high concentration feed solution increases current response in the system, which was observed at 30 mA (Fig. 5.a). High response current reduces overlap effect and causes an increase in the rate of ion transfer, which positively impacts the capacitance behavior and deionization capacity [63]. First principle calculations on adsorption behaviors have revealed that  $\text{NH}_3$  has a very small (more negative) adsorption energy ( $E_{\text{ads}}$ ) of -0.078 eV/atom, which results in strong interactions with  $\text{Ti}_3\text{C}_2\text{T}_x$  MXenes [64]. The calculations also show high charge transfer ( $C_t = 0.153$  e) between  $\text{NH}_3$  and  $\text{Ti}_3\text{C}_2\text{T}_x$ , hence solidifying the hypothesis that the high adsorption capacity is a consequence of chemisorption [64]. Further work is required to understand the kinetics of ammonia adsorption on  $\text{Ti}_3\text{C}_2\text{T}_x$  MXenes.

The adsorption rate values for the run are shown in Fig. 4.d. The average adsorption rate for AC is significantly lower ( $0.0021$  mg/min/cm<sup>2</sup>) than  $\text{Ti}_3\text{C}_2\text{T}_x$  ( $0.00545$  mg/min/cm<sup>2</sup>) owing to the lower plateau time and higher deionization efficiency of the later. It is interesting to note that the adsorption rate for AC changes very little across cycles, but it shows an upward trend for  $\text{Ti}_3\text{C}_2\text{T}_x$  (not including the first cycle). This is a consequence of decreasing plateau times for  $\text{Ti}_3\text{C}_2\text{T}_x$  electrodes. In batch system operation,  $C_o$  for each subsequent cycle is different. The value of  $C_o$  affects the kinetic accessibility of the dissolved ions, and hence has an effect on the adsorption rate. As discussed earlier, the regeneration efficiency of AC electrodes is marginally higher than  $\text{Ti}_3\text{C}_2\text{T}_x$  electrodes (Fig. 4.b). This manifests as consistent  $C_o$  and resultant adsorption rate for AC.

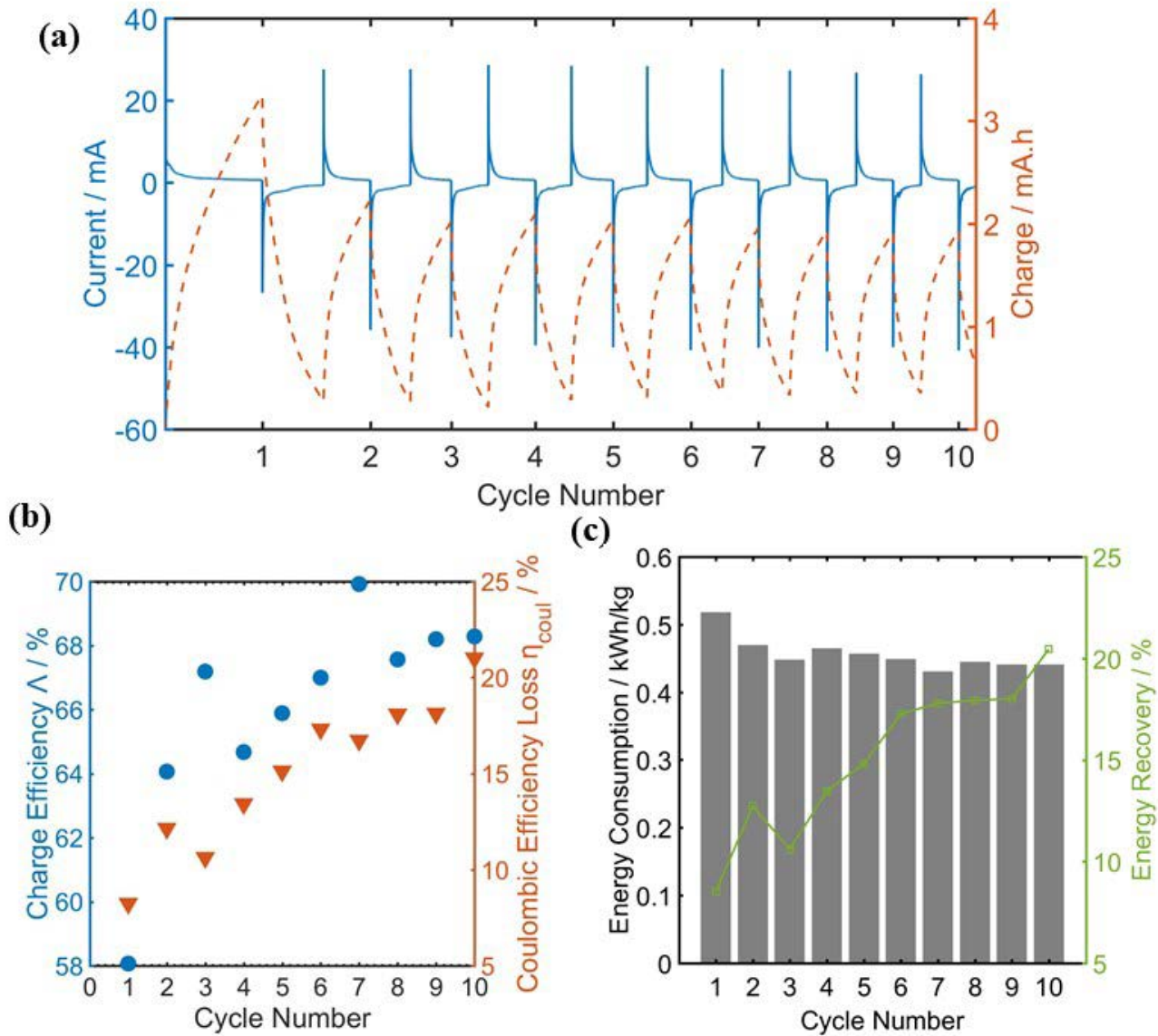


**Fig. 5. For each adsorption-desorption cycle: (a) Variation in current and charge; (b) Charge efficiency and Coulombic efficiency loss; (c) Energy consumption and recovery.**

The change in the current of the system is consistent with the change in the conductivity of the effluent solution. As shown in Fig. 5.a, the cell current decreases and total charge increases as ions are removed from the feed solution. During the discharging step, the current gradually rises back to its initial value, as partial charge is recovered. The charge efficiency ( $\Lambda$ ) and total Coulombic loss ( $\eta_{coul}$ ) in the system (Eq. 5, 6) are shown in Fig. 5.b. The values for  $\Lambda$  range from 58 to 70% over the course of the CDI test, while roughly increasing with each subsequent cycle. This is consistent with the observed trend of increasing adsorption rate for each cycle (Fig. 4.d),

as  $\lambda$  varies with varying  $C_o$  [65]. The reported values align well with results reported in literature [66]. A  $\lambda$  value of 100% has never been reported. It has been theorized that the relatively low  $\lambda$  values are an inherent consequence of pseudocapacitive behavior because of the presence of co-ion repulsion and counter-ion adsorption [66]. Some efforts have been made to increase the charge efficiency in CDI systems [67]. However, further work is needed in the area. The charge recovered during the discharging step is lower than the charge transferred during the charging step, resulting in a  $\eta_{\text{coul}}$  increasing from 8 to 21 % (Eq. 6, Fig. 5.b). This is a consequence of leakage current and is typical for supercapacitors and CDI systems. It should also be noted that current increases with each cycle (Fig. 5.a), which leads to more pronounced electrode polarization and hence results in an increase in  $\eta_{\text{coul}}$  with each cycle [32]. Pronounced electrode polarization is also responsible for decreasing deionization capacity (Fig. 3.4.c) [32]. Barring the first cycle, the energy consumption and recovery trends (Fig. 5.c) agree with  $\eta_{\text{coul}}$  and  $\lambda$ . This is in line with theoretical studies [67]. Energy recovery is defined as the ratio of recovered energy to consumed energy (Eq. 9). Over the course of ten cycles, 8 to 21% of energy was not recovered by the system. The profile closely resembles  $\eta_{\text{coul}}$ . The average energy consumption for the system was 0.45 kWh/kg. This is higher than the 0.24 kWh/kg obtained by Ma *et al.* [32] using  $\text{Ti}_3\text{C}_2$  films in flow-by CDI for NaCl removal. However, the deionization capacity achieved in this work is significantly higher. Hence, compensating for the marginally higher energy consumption. For comparison, commercial wastewater treatment plants require 4.6 kWh/kg of energy for ammonium ion removal [68]. This process requires ten times less energy, hence cementing the position of CDI as a green technology.

As shown in Table 1, materials such as activated carbon, graphite, and graphene have been studied for ammonia removal in FE-CDI systems [69], [54], [60], [70]. The deionization capacity shows several orders of magnitudes of improvement over 1.5 wt.% graphite [60]. It is apparent that  $\text{Ti}_3\text{C}_2\text{T}_x$  MXenes show markedly higher performance for ammonia removal when compared with previously researched electrode materials and systems.

Electrode Material	Ion Species	Cell Architecture	Applied Voltage (V)	Current	Initial Concentration (mg/L)	Deionization Efficiency (%)	Deionization Capacity (mg/g)	Reference
Ti <sub>3</sub> C <sub>2</sub> T <sub>x</sub> MXene	NaCl	Flow by	1.2	Constant Current – 20 mA	585	-	68	[51]
Porous Ti <sub>3</sub> C <sub>2</sub> T <sub>x</sub> MXene	NaCl	Flow by	1.2	-	10000	-	45	[52]
Ti <sub>3</sub> C <sub>2</sub> T <sub>x</sub> MXene	NaCl	Flow by	1.2	-	0.085	-	13	[54]
Ar-Ti <sub>3</sub> C <sub>2</sub> T <sub>x</sub> MXene	NaCl	Flow by	0.8 – 1.6	-	500	-	26.8	[55]
Graphene laminates	NH <sub>4</sub> Cl	Membrane Assisted	2	0.17 A	400	99	15.3	[71]
Graphite (1.5 wt%)	NH <sub>4</sub> Cl	Flow Electrode	0.2 – 1.2	-	20	87	1.43	[76]
Activated Carbon (0, 2, 5, 10 wt%)	NH <sub>4</sub> <sup>+</sup> -N	Flow Electrode	~ 0.8 V	Constant Current – 6 A/m <sup>2</sup>	43	95	-	[85]
Carbon Cloth	NH <sub>4</sub> Cl	Flow by	1.2 - 3	-	68.8	60.5–95.7	-	[86]
<b>Ti<sub>3</sub>C<sub>2</sub>T<sub>x</sub> MXene</b>	<b>NH<sub>4</sub>Cl</b>	<b>Flow Electrode</b>	<b>1.2</b>	<b>20 – 30 mA</b>	<b>500</b>	<b>60</b>	<b>460</b>	<b>This Work</b>

**Table 1. Comparison of performance metrics of different CDI technologies**

### 3.5. Conclusions

In this study, we demonstrated an FE-CDI system with remarkable ammonia removal performance based on flow electrodes consisting of Ti<sub>3</sub>C<sub>2</sub>T<sub>x</sub>MXene. A high average adsorption capacity of 460 mg/g along with a low energy consumption of 0.45 kWh/kg was witnessed. The results reinforce the strong dependence of FE-CDI performance on the characteristics of the electrode material. Owing to its high conductivity, colloidal stability, high surface area, and unique surface chemistry Ti<sub>3</sub>C<sub>2</sub>T<sub>x</sub> is a promising candidate for ammonia removal and recovery from industrial and commercial wastewaters.

While the results presented are promising, further research, including theoretical modelling of the ammonium ion interaction, kinetic analysis, and testing different MXenes is needed to further improve the process. Due to the nonuniform surface chemistry on MXene surfaces, it is important to consider how different etching approaches will change the adsorption process. Finally, MXenes have been shown as viable for many adsorption processes, but the studies are still in their infancy, Ti<sub>3</sub>C<sub>2</sub>T<sub>x</sub> and other MXenes should be tested for adsorption of more pollutants. However, based on these results, Ti<sub>3</sub>C<sub>2</sub>T<sub>x</sub> is among the most promising environmental remediation materials for ammonia removal from wastewater systems. We expect that the demonstrated work will open new avenues for realizing high performance, energy-efficient, large scale ammonia removal systems.

## Conflicts of Interest

There are no conflicts to declare.

## Acknowledgements

This work is funded in part by the Fulbright Fellowship Program and the Micron School of Materials Science at Boise State University. This work was supported through the Idaho National Laboratory (INL) Laboratory Directed Research & Development (LDRD) Program under DOE Idaho Operations Office Contract DE-AC07-05ID14517

## References

- [1] J. Macknick, R. Newmark, G. Heath, and K. C. Hallett, "Operational water consumption and withdrawal factors for electricity generating technologies: A review of existing literature," *Environ. Res. Lett.*, 2012, doi: 10.1088/1748-9326/7/4/045802.
- [2] DOE, "Energy demands on water resources," 2006.
- [3] I. E. A. IEA, "World Energy Outlook 2019 – Analysis - IEA," *World Energy Outlook 2019*, 2019. .
- [4] M. Palo, J. Uusivuori, G. Mery, A. V. Korotkov, and D. Humphreys, "World Forests, Markets and Policies: Towards a Balance," 2001.
- [5] C. Coyette, H.; Schenk, *Agriculture, forestry and fishery statistics*. 2019.
- [6] U.S Geological Survey, *Mineral Commodity Summaries 2020*. 2020.
- [7] W. J. Visek, "Ammonia: Its Effects on Biological Systems, Metabolic Hormones, and Reproduction," *J. Dairy Sci.*, 1984, doi: 10.3168/jds.S0022-0302(84)81331-4.
- [8] N. Gruber and J. N. Galloway, "An Earth-system perspective of the global nitrogen cycle," *Nature*. 2008, doi: 10.1038/nature06592.
- [9] U.S. EPA, "History of the clean water act," *EPA*. 2015.
- [10] R. R. Karri, J. N. Sahu, and V. Chimmiri, "Critical review of abatement of ammonia from wastewater," *Journal of Molecular Liquids*. 2018, doi: 10.1016/j.molliq.2018.03.120.
- [11] F. Jaramillo, M. Orchard, C. Muñoz, M. Zamorano, and C. Antileo, "Advanced strategies to improve nitrification process in sequencing batch reactors - A review," *Journal of*

- Environmental Management*. 2018, doi: 10.1016/j.jenvman.2018.04.019.
- [12] R. Semiat, "Energy issues in desalination processes," *Environmental Science and Technology*. 2008, doi: 10.1021/es801330u.
- [13] A. W. W. Association, *Reverse Osmosis and Nanofiltration (M46): AWWA Manual of Practice*, Second. 2007.
- [14] M. A. Ahmed and S. Tewari, "Capacitive deionization: Processes, materials and state of the technology," *Journal of Electroanalytical Chemistry*. 2018, doi: 10.1016/j.jelechem.2018.02.024.
- [15] K. Tang, Y.-H. Kim, S. Yiacoumi, and C. Tsouris, "(Invited) Capacitive Deionization of High-Salinity Water Using Ion-Exchange Membranes," *{ECS} Meet. Abstr.*, 2017, doi: 10.1149/ma2017-02/22/1032.
- [16] F. A. AlMarzooqi, A. A. Al Ghaferi, I. Saadat, and N. Hilal, "Application of Capacitive Deionisation in water desalination: A review," *Desalination*. 2014, doi: 10.1016/j.desal.2014.02.031.
- [17] Y. Oren, "Capacitive deionization (CDI) for desalination and water treatment - past, present and future (a review)," *Desalination*, 2008, doi: 10.1016/j.desal.2007.08.005.
- [18] W. Tang *et al.*, "Various cell architectures of capacitive deionization: Recent advances and future trends," *Water Research*. 2019, doi: 10.1016/j.watres.2018.11.064.
- [19] P. M. Biesheuvel, B. van Limpt, and A. van der Wal, "Dynamic Adsorption/Desorption Process Model for Capacitive Deionization," *J. Phys. Chem. C*, vol. 113, no. 14, pp. 5636–5640, Apr. 2009, doi: 10.1021/jp809644s.
- [20] E. M. Remillard, A. N. Shocron, J. Rahill, M. E. Suss, and C. D. Vecitis, "A direct comparison of flow-by and flow-through capacitive deionization," *Desalination*, 2018, doi: 10.1016/j.desal.2018.01.018.
- [21] S. Dahiya and B. K. Mishra, "Enhancing understandability and performance of flow electrode capacitive deionisation by optimizing configurational and operational parameters: A review on recent progress," *Separation and Purification Technology*. 2020, doi: 10.1016/j.seppur.2020.116660.
- [22] P. Ratajczak, M. E. Suss, F. Kaasik, and F. Béguin, "Carbon electrodes for capacitive

- technologies," *Energy Storage Mater.*, vol. 16, pp. 126–145, 2019, doi: <https://doi.org/10.1016/j.ensm.2018.04.031>.
- [23] M. A. Luciano, H. Ribeiro, G. E. Bruch, and G. G. Silva, "Efficiency of capacitive deionization using carbon materials based electrodes for water desalination," *J. Electroanal. Chem.*, vol. 859, p. 113840, 2020, doi: <https://doi.org/10.1016/j.jelechem.2020.113840>.
- [24] K. Y. Choo, C. Y. Yoo, M. H. Han, and D. K. Kim, "Electrochemical analysis of slurry electrodes for flow-electrode capacitive deionization," *J. Electroanal. Chem.*, 2017, doi: [10.1016/j.jelechem.2017.10.040](https://doi.org/10.1016/j.jelechem.2017.10.040).
- [25] G. Deysher *et al.*, "Synthesis of Mo<sub>4</sub>VAIC<sub>4</sub> MAX Phase and Two-Dimensional Mo<sub>4</sub>VC<sub>4</sub> MXene with Five Atomic Layers of Transition Metals," *ACS Nano*, 2020, doi: [10.1021/acsnano.9b07708](https://doi.org/10.1021/acsnano.9b07708).
- [26] C. E. Shuck *et al.*, "Scalable Synthesis of Ti<sub>3</sub>C<sub>2</sub>T<sub>x</sub> MXene," *Adv. Eng. Mater.*, vol. 22, no. 3, p. 1901241, 2020, doi: [10.1002/adem.201901241](https://doi.org/10.1002/adem.201901241).
- [27] K. Maleski, V. N. Mochalin, and Y. Gogotsi, "Dispersions of Two-Dimensional Titanium Carbide MXene in Organic Solvents," *Chem. Mater.*, 2017, doi: [10.1021/acs.chemmater.6b04830](https://doi.org/10.1021/acs.chemmater.6b04830).
- [28] Y. Zhang, L. Wang, N. Zhang, and Z. Zhou, "Adsorptive environmental applications of MXene nanomaterials: A review," *RSC Advances*. 2018, doi: [10.1039/c8ra03077d](https://doi.org/10.1039/c8ra03077d).
- [29] G. Liu *et al.*, "Ultrathin two-dimensional MXene membrane for pervaporation desalination," *J. Memb. Sci.*, 2018, doi: [10.1016/j.memsci.2017.11.065](https://doi.org/10.1016/j.memsci.2017.11.065).
- [30] M. Naguib *et al.*, "Two-Dimensional Nanocrystals: Two-Dimensional Nanocrystals Produced by Exfoliation of Ti<sub>3</sub>AlC<sub>2</sub> (Adv. Mater. 37/2011)," *Adv. Mater.*, 2011, doi: [10.1002/adma.201190147](https://doi.org/10.1002/adma.201190147).
- [31] G. K. Nasrallah, M. Al-Asmakh, K. Rasool, and K. A. Mahmoud, "Ecotoxicological assessment of Ti<sub>3</sub>C<sub>2</sub>T<sub>x</sub>:X (MXene) using a zebrafish embryo model," *Environ. Sci. Nano*, 2018, doi: [10.1039/c7en01239j](https://doi.org/10.1039/c7en01239j).
- [32] J. Ma, Y. Cheng, L. Wang, X. Dai, and F. Yu, "Free-standing Ti<sub>3</sub>C<sub>2</sub>T<sub>x</sub> MXene film as binder-free electrode in capacitive deionization with an ultrahigh desalination capacity," *Chem. Eng. J.*, 2020, doi: [10.1016/j.cej.2019.123329](https://doi.org/10.1016/j.cej.2019.123329).

- [33] W. Bao *et al.*, "Porous Cryo-Dried MXene for Efficient Capacitive Deionization," *Joule*, 2018, doi: 10.1016/j.joule.2018.02.018.
- [34] L. Agartan *et al.*, "Influence of operating conditions on the desalination performance of a symmetric pre-conditioned Ti<sub>3</sub>C<sub>2</sub>T<sub>x</sub>-MXene membrane capacitive deionization system," *Desalination*, vol. 477, p. 114267, 2020, doi: <https://doi.org/10.1016/j.desal.2019.114267>.
- [35] P. Srimuk *et al.*, "MXene as a novel intercalation-type pseudocapacitive cathode and anode for capacitive deionization," *J. Mater. Chem. A*, 2016, doi: 10.1039/c6ta07833h.
- [36] L. Guo, X. Wang, Z. Y. Leong, R. Mo, L. Sun, and H. Y. Yang, "Ar plasma modification of 2D MXene Ti<sub>3</sub>C<sub>2</sub>T<sub>x</sub> nanosheets for efficient capacitive desalination," *FlatChem*, 2018, doi: 10.1016/j.flatc.2018.01.001.
- [37] S. Venkateshalu and A. N. Grace, "MXenes—A new class of 2D layered materials: Synthesis, properties, applications as supercapacitor electrode and beyond," *Applied Materials Today*. 2020, doi: 10.1016/j.apmt.2019.100509.
- [38] B. Anasori, M. R. Lukatskaya, and Y. Gogotsi, "2D metal carbides and nitrides (MXenes) for energy storage," *Nature Reviews Materials*. 2017, doi: 10.1038/natrevmats.2016.98.
- [39] Y. Y. Peng *et al.*, "All-MXene (2D titanium carbide) solid-state microsupercapacitors for on-chip energy storage," *Energy Environ. Sci.*, 2016, doi: 10.1039/c6ee01717g.
- [40] X. Zhang, Z. Zhang, and Z. Zhou, "MXene-based materials for electrochemical energy storage," *Journal of Energy Chemistry*. 2018, doi: 10.1016/j.jechem.2017.08.004.
- [41] A. K. Shukla, A. Banerjee, M. K. Ravikumar, and A. Jalajakshi, "Electrochemical capacitors: Technical challenges and prognosis for future markets," *Electrochimica Acta*. 2012, doi: 10.1016/j.electacta.2012.03.059.
- [42] P. Simon and Y. Gogotsi, "Materials for electrochemical capacitors," *Nature Materials*. 2008, doi: 10.1038/nmat2297.
- [43] R. Malik, "Maxing Out Water Desalination with MXenes," *Joule*. 2018, doi: 10.1016/j.joule.2018.04.001.
- [44] Y. Zhao, Y. Wang, R. Wang, Y. Wu, S. Xu, and J. Wang, "Performance comparison and energy consumption analysis of capacitive deionization and membrane capacitive deionization processes," *Desalination*. 2013, doi: 10.1016/j.desal.2013.06.009.

- [45] K. Maleski, C. E. Ren, M. Q. Zhao, B. Anasori, and Y. Gogotsi, "Size-Dependent Physical and Electrochemical Properties of Two-Dimensional MXene Flakes," *ACS Appl. Mater. Interfaces*, 2018, doi: 10.1021/acsami.8b04662.
- [46] C. E. Shuck *et al.*, "Effect of Ti<sub>3</sub>AlC<sub>2</sub> MAX Phase on Structure and Properties of Resultant Ti<sub>3</sub>C<sub>2</sub>T<sub>x</sub> MXene," *ACS Appl. Nano Mater.*, 2019, doi: 10.1021/acsanm.9b00286.
- [47] S. A. Hawks *et al.*, "Performance metrics for the objective assessment of capacitive deionization systems," *Water Research*. 2019, doi: 10.1016/j.watres.2018.10.074.
- [48] K. Singh, S. Porada, H. D. de Gier, P. M. Biesheuvel, and L. C. P. M. de Smet, "Timeline on the application of intercalation materials in Capacitive Deionization," *Desalination*. 2019, doi: 10.1016/j.desal.2018.12.015.
- [49] M. Lu, W. Han, H. Li, W. Zhang, and B. Zhang, "There is plenty of space in the MXene layers: The confinement and fillings," *J. Energy Chem.*, 2020, doi: 10.1016/j.jechem.2020.02.032.
- [50] A. Sarycheva and Y. Gogotsi, "Raman Spectroscopy Analysis of the Structure and Surface Chemistry of Ti<sub>3</sub>C<sub>2</sub>T<sub>x</sub> MXene," *Chem. Mater.*, vol. 32, no. 8, pp. 3480–3488, Apr. 2020, doi: 10.1021/acs.chemmater.0c00359.
- [51] M. R. Lukatskaya *et al.*, "Ultra-high-rate pseudocapacitive energy storage in two-dimensional transition metal carbides," *Nat. Energy*, 2017, doi: 10.1038/nenergy.2017.105.
- [52] M. N. Rahaman, *Ceramic processing*. 2017.
- [53] K. Fang, H. Gong, W. He, F. Peng, C. He, and K. Wang, "Recovering ammonia from municipal wastewater by flow-electrode capacitive deionization," *Chem. Eng. J.*, 2018, doi: 10.1016/j.cej.2018.04.128.
- [54] Y. Wimalasiri, M. Mossad, and L. Zou, "Thermodynamics and kinetics of adsorption of ammonium ions by graphene laminate electrodes in capacitive deionization," *Desalination*, 2015, doi: 10.1016/j.desal.2014.11.015.
- [55] S. Porada, R. Zhao, A. Van Der Wal, V. Presser, and P. M. Biesheuvel, "Review on the science and technology of water desalination by capacitive deionization," *Progress in Materials Science*. 2013, doi: 10.1016/j.pmatsci.2013.03.005.

- [56] X. Sang *et al.*, "Atomic defects in monolayer titanium carbide (Ti<sub>3</sub>C<sub>2</sub>T<sub>x</sub>) MXene," *ACS Nano*, 2016, doi: 10.1021/acsnano.6b05240.
- [57] T. Habib *et al.*, "Oxidation stability of Ti<sub>3</sub>C<sub>2</sub>T<sub>x</sub> MXene nanosheets in solvents and composite films," *npj 2D Mater. Appl.*, 2019, doi: 10.1038/s41699-019-0089-3.
- [58] Y. Lee *et al.*, "Oxidation-resistant titanium carbide MXene film," *J. Mater. Chem. A*, 2019, doi: 10.1039/C9TA07036B.
- [59] V. Natu, R. Pai, M. Sokol, M. Carey, V. Kalra, and M. W. Barsoum, "2D Ti<sub>3</sub>C<sub>2</sub>T<sub>z</sub> MXene Synthesized by Water-free Etching of Ti<sub>3</sub>AlC<sub>2</sub> in Polar Organic Solvents," *Chem*, 2020, doi: 10.1016/j.chempr.2020.01.019.
- [60] M. Seredych and T. J. Bandoz, "Removal of ammonia by graphite oxide via its intercalation and reactive adsorption," *Carbon*. 2007, doi: 10.1016/j.carbon.2007.06.007.
- [61] S. Wang, H. Sun, H. M. Ang, and M. O. Tadé, "Adsorptive remediation of environmental pollutants using novel graphene-based nanomaterials," *Chemical Engineering Journal*. 2013, doi: 10.1016/j.cej.2013.04.070.
- [62] D. Moreno and M. C. Hatzell, "Influence of Feed-Electrode Concentration Differences in Flow-Electrode Systems for Capacitive Deionization," *Ind. Eng. Chem. Res.*, 2018, doi: 10.1021/acs.iecr.8b01626.
- [63] Y. Li *et al.*, "A protic salt-derived porous carbon for efficient capacitive deionization: Balance between porous structure and chemical composition," *Carbon N. Y.*, 2017, doi: 10.1016/j.carbon.2017.01.084.
- [64] M. Wu *et al.*, "Ti<sub>3</sub>C<sub>2</sub> MXene-Based Sensors with High Selectivity for NH<sub>3</sub> Detection at Room Temperature," *ACS Sensors*, 2019, doi: 10.1021/acssensors.9b01308.
- [65] P. M. Biesheuvel, S. Porada, M. Levi, and M. Z. Bazant, "Attractive forces in microporous carbon electrodes for capacitive deionization," *J. Solid State Electrochem.*, 2014, doi: 10.1007/s10008-014-2383-5.
- [66] T. Kim, J. E. Dykstra, S. Porada, A. van der Wal, J. Yoon, and P. M. Biesheuvel, "Enhanced charge efficiency and reduced energy use in capacitive deionization by increasing the discharge voltage," *J. Colloid Interface Sci.*, 2015, doi: 10.1016/j.jcis.2014.08.041.

- [67] X. Gao, A. Omosebi, J. Landon, and K. Liu, "Enhancement of charge efficiency for a capacitive deionization cell using carbon xerogel with modified potential of zero charge," *Electrochem. commun.*, 2014, doi: 10.1016/j.elecom.2013.12.004.
- [68] M. Ekman, B. Björleinius, and M. Andersson, "Control of the aeration volume in an activated sludge process using supervisory control strategies," *Water Res.*, 2006, doi: 10.1016/j.watres.2006.02.019.
- [69] C. Zhang, J. Ma, and T. D. Waite, "Ammonia-Rich Solution Production from Wastewaters Using Chemical-Free Flow-Electrode Capacitive Deionization," *ACS Sustain. Chem. Eng.*, 2019, doi: 10.1021/acssuschemeng.9b00314.
- [70] Z. Ge, X. Chen, X. Huang, and Z. J. Ren, "Capacitive deionization for nutrient recovery from wastewater with disinfection capability," *Environ. Sci. Water Res. Technol.*, 2018, doi: 10.1039/c7ew00350a.

